Journal of Materials Science & Technology 105 (2022) 194–202

Contents lists available at ScienceDirect

Journal of Materials Science & Technology

journal homepage: www.elsevier.com/locate/jmst

Research Article

Highly flexible and compressible polyimide/silica aerogels with integrated double network for thermal insulation and fire-retardancy

Jing Tian[a], Yi Yang[a], Tiantian Xue[a], Guojie Chao[a,b], Wei Fan[a,*], Tianxi Liu[a,b,*]

[a] State Key Laboratory for Modification of Chemical Fibers and Polymer Materials, College of Materials Science and Engineering, Donghua University, Shanghai 201620, China
[b] Key Laboratory of Synthetic and Biological Colloids, Ministry of Education, School of Chemical and Material Engineering, Jiangnan University, Wuxi 214122, China

ARTICLE INFO

Article history:
Received 14 May 2021
Revised 6 July 2021
Accepted 7 July 2021
Available online 20 September 2021

Keywords:
Polyimide
Silica
Aerogel
Thermal insulation
Fire-retardancy

ABSTRACT

The materials with thermal insulating and fire-retardant properties are highly demanded for architectures to improve the energy efficiency. The applications of conventional inorganic insulating materials such as silica aerogels are restricted by their mechanical fragility and organic insulating materials are either easily ignitable or exhibit unsatisfactory thermal insulation performance. Here, we report an organic/inorganic composite aerogel with integrated double network structure, in which silica constituent homogeneously distribute in the anisotropic polyimide nanofiber aerogel matrix and strong interfacial effect is formed between two components. The integrated binary network endows the polyimide/silica composite aerogels with outstanding compressibility and flexibility even with a high inorganic content of 60%, which can withstand 500 cyclic fatigue tests at a compressive strain of 50% in the radial direction. The resulting composite aerogel exhibits a combination of outstanding insulating performance with a low thermal conductivity (21.2 mW m^{-1} K^{-1}) and excellent resistance to a 1200°C flame without disintegration. The high-performance polyimide/silica aerogels can decrease the risk brought by the collapse of reinforced concrete structures in a fire, demonstrating great potential as efficient building materials.

1. Introduction

It is reported that the energy needed to regulate the indoor temperature of buildings accounts for about 20% of the world's energy consumption and produces about 30% of greenhouse gas emissions [1]. In order to promote sustainable development, materials with superior insulation performance for energy efficient buildings need to be developed. However, most commercial insulating materials always exhibit greatly increased thermal conductivities in humid environments, such as polyurethane (PUR) foams (84% increasement from 25 mW m^{-1} K^{-1} to 46 mW m^{-1} K^{-1}), expanded polystyrene (EPS) (50% increasement from 36 mW m^{-1} K^{-1} to 54 mW m^{-1} K^{-1}) and glass wool (49% increasement from 37 mW m^{-1} K^{-1} to 55 mW m^{-1} K^{-1}) with an increasing relative humidity of 10% [2]. In addition, the polymeric foams are always highly combustible and can spread the fire rapidly, increasing the safety hazard of architectures [3]. Unfortunately, the addition of halogenated or phosphorous flame retardants has been restricted by international environmental organizations because these additives tend to release toxic substances that are harmful to the environment and humans [4]. Therefore, it is necessary to develop a kind of insulation material with good thermal insulating performance as well as mechanical robustness or resilient, moisture-resistant and fire-retardant properties.

Aerogels display great potential for thermal insulation applications owing to their low density and high porosity [5]. However, traditional inorganic aerogels such as silica aerogels tend to show mechanical brittleness despite their ultra-low thermal conductivity. Although some high-performance inorganic aerogels previously reported such as ceramic nanofibrous aerogels, ceramic nanowire aerogels and hyperbolic ceramic aerogels displayed excellent mechanical elasticity, the complex preparation process and the harsh treatment conditions prevent their large-scale applications [6-8]. Unlike inorganic aerogels, polymer aerogels with better mechanical performance can always be prepared by a cost-efficient manufacturing process. However, typical organic aerogels such as poly(vinyl alcohol) aerogels and cellulose aerogels tend to exhibit inferior heat stability with decomposition temperature of 100~200°C and will quickly spread the flame and shrink severely once be ignited [9,10]. It has shown that the incorporation of inorganic nanofillers, such as silica, graphene, carbon nanotubes, clays and their hybrids into the polymer matrix can introduce a large

* Corresponding authors.
E-mail addresses: weifan@dhu.edu.cn (W. Fan), txliu@fudan.edu.cn, txliu@dhu.edu.cn (T. Liu).

https://doi.org/10.1016/j.jmst.2021.07.030
1005-0302/

amount of phonon barriers [10-14], thus greatly reducing the solid heat conduction of materials. In addition, the thermal stability and fire resistance of the polymer materials can also be improved simultaneously [15,16]. Therefore, designing and fabricating organic-inorganic composite aerogels is an efficient method to significantly improve the flame-resistant properties for thermal shielding buildings.

Compared with most organic materials, polyimide (PI) shows superior thermal stability, mechanical strength and self-extinguishing performance due to the rigid imide rings on the main backbone [17,18]. A series of polyimide-based materials such as PI/graphene composites, PI/boron nitride composites, and isocyanate-based PI foams have realized excellent thermal and fire resistance [19-21]. Polyimide (PI) aerogels, which inherit the comprehensive properties of PI, are attractive for their outstanding mechanical properties, low thermal conductivity, good thermal stability at a wide temperature range (250∼450°C), exhibiting enormous potential for applications in military and spaceflight [22,23]. Previous studies have revealed that PI nanofibrous aerogels can display great potential for outstanding thermal insulating materials due to their extraordinary flexibility and elasticity, low density and ultra-low thermal conductivity of ∼0.040 W $m^{-1}K^{-1}$ [24,25]. Unfortunately, higher temperature, especially the flame would cause thermal oxidation damage to PI aerogels, resulting in rapid degradation, volume shrinkage and structural failure. In order to further improve the thermal insulating and fire-retardant performance of PI aerogels, previous reports have shown that introducing inorganic constituent to fabricate polyimide composite aerogels is an efficient way [26-28]. However, incorporating inorganic fillers into polymer aerogels usually increases the density of hybrids. Weak interfacial interactions among fillers and the polymer matrix can still tend to bring about heavier aggregations and eventual degradation of mechanical robustness [29-31]. Therefore, how to regulate and optimize the interfacial interaction between fillers and polyimide matrix through efficient preparation method is the key to obtain organic-inorganic composite aerogels with comprehensive performance [30,32,33]. Although some previous methods such as the “co-gel” strategy was beneficial for the fabrication of homogeneous silica/polyimide nanocomposite aerogels with enhanced compressive modulus and flame resistance, this material failed to overcome the inherent brittleness of silica, which was lack of compression resilience [34]. To our knowledge, the flexible and compressible polyimide/silica composite aerogels have not been reported yet [23,34-36]. Therefore, endowing polyimide/silica composite aerogels with flexibility instead of sacrificing the thermal insulting performance of the composites is a challenge.

Herein, we design a flexible and compressible polyimide/silica (PSi) composite aerogel with integrated double network by an in-situ synthesis strategy, using anisotropic polyimide nanofiber aerogel (PINA) as a template for the growth of continuous silica network. During the polycondensation process, hydrogen bonds between the polymethylsilsesquioxane (PMSQ) oligomers and PI chains facilitated the homogeneous distribution of PMSQ colloidal nanoparticles, resulting in the formation of continuous SiO_2 and PINA double network. Because of the integrated anisotropic structure, the composite aerogel is mechanically resilient and could withstand 500 cyclic fatigue tests at a compressive strain of 50% without fracture in the radial direction and mechanically robust in the axial direction. Additionally, the PSi composite aerogel exhibits an ultra-low thermal conductivity of 20.3∼27.5 mW m^{-1} K^{-1} in the radial direction, which is lower than most organic aerogels like cellulose aerogels and hybrid aerogels like phenolic-silica aerogels [9,37]. Profit from the robust interfacial interactions among PINA matrix and silica network, the composite aerogel exhibits excellent flame-retardant performance and the stability to sustain a flame of ultra-high temperature without collapse even during the consumption of organic component.

2. Experimental

2.1. Materials

Triethylamine (TEA), N, N-dimethylacetamide (DMAc), methyltrimethoxysilane (MTMS), cetyltrimethylammonium bromide (CTAB), urea, alcohol (99%) and acetic acid (99%) were supplied by Sinopharm Chemical Reagent Co.

2.2. Fabrication of polyimide nanofiber aerogels (PINAs)

The water-soluble poly(amic acid) (PAA) was fabricated by polycondensation of pyromellitic dianhydride (PMDA) and 4,4'-oxidianiline (ODA) and the PAA nanofibers were prepared through electrospinning process according to our previous work [23,27,38]. 500 mg PAA nanofibers were subsequently dispersed in 100 ml PAA solution with the content of 0.5 wt% by a homogenizer (IKA T25, Germany) for 20 min at 11,000 rpm. Afterwards, the uniform dispersions were transferred into the molds and placed on a copper block that was immersed in liquid nitrogen bath to apply unidirectional freezing. Finally, the samples were freeze-dried for 72 h and then thermally imidized under an air atmosphere at 150°C and 300°C for 1 h respectively to obtain the PINAs.

2.3. Preparation of polyimide/silica (PSi) composite aerogels

First, 0.5 ml of MTMS was slowly added in a mixture with 15 ml of acetic acid aqueous solution (1×10^{-2} M), 0.5 g of urea and 0.09 g of CTAB at room temperature. The mixture was stirred for 30 min to obtain a hydrolyzed MTMS solution. The PINA was then immersed into the above hydrolyzed MTMS solution and a further hydrolytic polycondensation process (80°C, 8 h) occurred with a secondary PMSQ network generated on the PINA matrix. After the reaction was completed, the composite was freeze-dried for 48 h, followed by a thermal treatment process (N_2, 250°C, 1 h) to obtain the PSi composite aerogel. A series of PSi composite aerogels with inorganic content of 0, 20%, 40%, 60% and 80% were denoted as PSi-0, PSi-2, PSi-4, PSi-6 and PSi-8, respectively.

2.4. Characterization

The microstructures of the PSi aerogels were investigated by field-emission scanning electron microscopy (FE-SEM-EDS, JSM-7500F, JEOL, Japan) and transmission electron microscopy (TEM, JEM-2100, JEOL). Pore size distributions of aerogels were characterized on a capillary flow porometer (CFP-1500AEX, Porous Materials Inc., USA). A Nicolet-8700 infrared spectrometer from Nicolet (USA) was used to measure ATR-FTIR spectra of the samples. Thermogravimetric analysis (TGA) was performed on a TGA instrument (F1 Libra, Netzsch Co., Ltd, German) under an air/nitrogen flow. The derivative thermogravimetric (DTG) curves were obtained by the first derivative of TG curves. The compressive tests were performed on an electronic universal testing machine (UTM2102, Suns Technology Stock Co., Ltd, China) equipped with a 200 N sensor at a strain rate of 10 mm min^{-1}. Thermal conductivity was detected on a hot disk thermal analyzer (Hot Disk TPS 2500S, Sweden) according to the transient plane source method (ISO 22007-2:2015). Thermographic images were recorded by an infrared thermal camera (FOTRIC 220S, China). The water contact angle of the aerogels was measured by a contact angle analyzer (OCA40Micro, China). A microscale combustion calorimeter device (MCC-2, Govmark, USA)

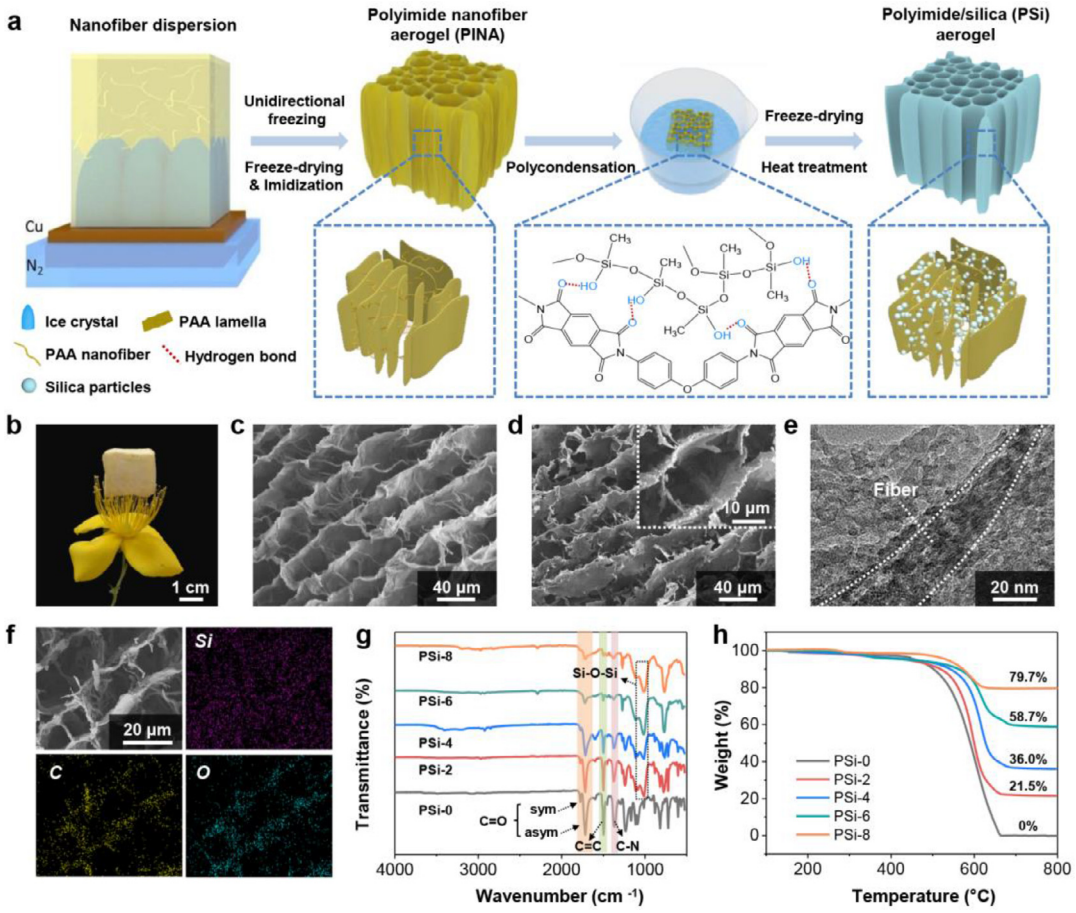

Fig. 1. Preparation, structure characterization and composition of PSi aerogels. (a) Schematic illustration of the structure design of PSi aerogels. (b) Optical photograph of PSi-6 aerogel with a volume of 8.6 cm^3 standing on the stamens of a flower without bending them. SEM images of (c) PSi-0 and (d) PSi-6 aerogels demonstrating the multi-scale architecture. (e) TEM image of PSi-6 aerogel demonstrating the homogeneous distribution of the silica constituents. (f) SEM-EDS images of PSi-6 aerogel. (g) FT-IR spectra of PSi aerogels. (h) TGA curves of PSi aerogels demonstrating the respective content of silica.

was used to investigate the combustion behavior of aerogels according to ASTM D7309-2007. The porosity (P) of the aerogel can be calculated according to Equation (1):

$$P = \left(1 - \frac{\rho_0}{\rho}\right) \times 100\%, \quad (1)$$

where P is the porosity, ρ_0 is the apparent density of the aerogel, and ρ is the volume density of polymer, which is estimated from the weighted average of densities of SiO_2 (2.20 g cm^{-3}) and PI (1.38 g cm^{-3}).

3. Results and discussion

The polyimide/silica (PSi) composite aerogel was achieved by employing polyimide nanofiber aerogel (PINA) matrix as a template for the in-situ growth of polymethylsilsesquioxane (PMSQ) network followed by thermal treatment (Fig. 1(a)). Briefly, the preparation process began with the fabrication of unidirectional anisotropic polyimide nanofiber aerogel (PINA). First, the electrospun poly(amic acid) (PAA) nanofibers were dispersed homogeneously with PAA sol in water. Followed by unidirectional freeze-drying and thermal imidization, the PINA with unidirectional anisotropic structure can be obtained. Then, the as-prepared PINA was immersed into the acid hydrolyzed methyltrimethoxysilane (MTMS) solution containing cetyltrimethylammonium bromide (CTAB) and uera. Hydrogen bonds between the PMSQ oligomers and PI chains facilitated the homogeneous distribution of PMSQ colloidal nanoparticles, resulting in the formation of two continuous networks [39]. Followed by freeze-drying and heat treatment, the PSi composite aerogel with integrated double network structure was successfully obtained. The density and porosity of PSi-x aerogels are shown in Fig. S1. The PSi-6 aerogel still displayed a low density (0.046 g cm^{-3}) and a high porosity (97.6%) even when the inorganic content reached 60%. Fig. 1(b) shows that a typical PSi-6 (8.6 cm^3) with a low density can be placed on the tip of stamens of a flower without bending them, highlighting the ultralight feature of the PSi composite aerogel.

As illustrated by the SEM image in Fig. 1(c), PINA exhibits a hierarchical and fiber-connected-lamellar porous structure due to the unidirectional freezing technique. The PSi-6 aerogel perfectly remains the anisotropic structure of the PINA matrix and exhibits a multi-scale structure, as shown in Fig. 1(d). The SiO_2 constituents widely and homogeneously disperse within PINA networks, which can be indicated by the increase of surface roughness of lamellas and nanofibers in the inset, suggesting a good affinity between the SiO_2 networks and the PINA matrix. The TEM image in Fig. 1(e) corroborates the homogeneous distribution of the SiO_2 constituents on lamellas and nanofibers down to the nanoscale. The SEM-EDS maps (Fig. 1(f)) of PSi-6 aerogel also illustrate the uniform distribution of Si, C and O elements, indicating the homogeneity of the inorganic constituent in PINA matrix. Such uniformity of the PSi aerogel is due to the in-situ generation of PMSQ nanoparticles in PINA matrix. Briefly, the anisotropic multi-scale structure of PSi aerogel is demonstrated at different length scales. i) The SiO_2 domains are distributed in the PINA matrix uniformly

at the nanoscale, resulting in the outstanding structural stability and integrity of the composite aerogel. ii) The micron-sized fiber-connected-lamellar cellular structure could effectively transfer stress. iii) Anisotropic structural design is beneficial to the high stiffness in the axial direction and compressive resilience in the radial direction of the composite aerogel. Constructing such architecture with integrated flexible PINA network and rigid SiO_2 network is an effective approach to achieve composites with high strength, elasticity and outstanding mechanical stability. The morphology of composite aerogels with different contents of silica is illustrated in Fig. S2(a). With the increase of organic content, the structure of PSi aerogels become denser until the layered structure cannot be found obviously in PSi-8. As shown in Fig. S2(b), PSi-0 aerogel exhibits large pore sizes ranging from 20 to120 μm with a wide distribution. With the load of silica on the PI lamellas, the composite aerogels exhibit smaller pore sizes (center in ~15 μm for PSi-6) and more uniform distributions. Of course, the density of PSi aerogels also increases significantly from 0.010 g cm^{-3} of PSi-0 to 0.114 g cm^{-3} of PSi-8.

As illustrated in FT-IR spectra of PSi aerogels in Fig. 1(g), the characteristic peaks located at1370 cm^{-1}(C–N stretching vibrations), 1490 cm^{-1} (C=C stretching vibrations), 1716 cm^{-1} and 1776 cm^{-1} (C=O symmetric and asymmetric stretching vibration) could be observed in all samples, which were typical peaks of polyimide [34]. The peaks of the Si–O–Si groups were located at 1010 cm^{-1} with the enhanced strength from PSi-2 to PSi-8, which is attributed to the increase of the inorganic constituent. The shift of the C=O peak from 1716 cm^{-1} for PSi-0 to1720 cm^{-1} for PSi-6 may be attributed to the inductive effect between Si–O–Si groups on silica network and C=O groups in PINA matrix, due to hydrogen bonds existed between C=O groups in the PI aerogels and Si-OH groups in the PMSQ oligomers. The FT-IR spectrum in Fig. S3 illustrated that there are no obvious peaks of –OH at 3340 cm^{-1} and $-CH_3$ at 2970 cm^{-1} after heat treatment, which indicated that the PMSQ were converted into SiO_2 [40]. The TGA curves of PSi aerogels are shown in Fig. 1(h). The inorganic content of PSi aerogels was correlated with the amount of MTMS added, which can be controlled to 21.5% (PSi-2), 36.0% (PSi-3), 58.7% (PSi-6), and 79.7% (PSi-8) respectively. A shift of the peak on DTG curves from 602°C for PSi-0 to 618°C for PSi-6 aerogel further proves the improvement of the thermal stability of the composite materials with the combination of silica (Fig. S4).

Because of the anisotropic structures of the PSi aerogels, compression tests were performed respectively in the axial (parallel to the freezing direction) and radial (perpendicular to the freezing direction) directions, as illustrated in Fig. 2(a). Fig. 2(b) shows the stress-strain (σ-ε) curves of PSi-6 aerogels in the two directions. The PSi-6 aerogel exhibits a stiff deformation behavior in the axial direction, including four characteristic stages: a linear elastic behavior at ε <5%, a nonlinear elastic region of 5% < ε < 20%, a relative flat plateau region for 20% < ε < 50%, and a final densification behavior for ε > 50%. While no apparent yielding plateau is observed and the maximum stress at 80% strain is lower when compressed in the radial direction. Such anisotropic mechanical behavior is mainly attributed to the microstructure anisotropy of aerogels, that the vertically arranged lamellas can withstand high load in the axial direction, which is similar to other anisotropic aerogel materials reported previously [41-43]. Due to the increase of inorganic content, the Young's modulus shows obvious improvement (Fig. 2(c)), and the PSi-6 aerogel displays a high Young's modulus of 100 kPa in the axial direction, which is 10 times higher than the PSi-0 aerogel. The difference between axial and radial modulus becomes greater as the inorganic content increases, demonstrating the higher mechanical anisotropy of the composite aerogels, which is attributed to the more rigid lamellas obtained via the combination of SiO_2 network. However, by further increasing the inorganic content, PSi-8 aerogel disintegrated under compression due to the intrinsic brittleness of silica (Fig. S5).

Unlike the stiff and brittle character of other polymer/silica hybrid aerogels reported in the previous works [44,45], the PSi-6 aerogel exhibited mechanical flexibility in the radial direction, recovering from large compression (ε = 60%) without collapse (insets in Fig. 2(d) and Movie S1). The stress-strain curves (Fig. 2(d)) exhibit the excellent compression recovery properties of PSi-6 aerogel from different strain (15%, 30%, 45% and 60%). This resilient compressibility in radial direction also exhibited a durable cycling performance (Movie S1), with a slight plastic deformation of 6% after 500 fatigue cycles at a compressive strain of 50% (Fig. 2(e)). However, the aerogels with oriented arranged lamellas reported previously tend to exhibit a large plastic deformation (> 10%), which may be attributed to the lack of interlamellar connection to transfer stress [46-48]. Fig. 2(f) shows the variations of maximum stress, Young's modulus and energy loss coefficient of PSi-6 aerogels during the cyclic compressive process. Over 65% of the initial maximum stress has been remained after 500 compressive cycles, demonstrating the structural robustness of PSi-6 aerogels. We thus believe the novel structure with flexible nanofibers bonded lamellas will endow the PSi aerogels with structural robustness and high elasticity. The extraordinary compressibility of PSi-6 aerogels is ascribed to their anisotropic structure with integrated double network, and the illustration is shown in Fig. 2(g). When the aerogel is compressed, the stress is dispersed through the nanofibers to avoid local stress concentration. Once the applied load is released, these bended nanofibers can recover to their initial shapes, thus supporting the bulk aerogel for a complete recovery [49]. Moreover, the repulsive interactions between residual alkyl groups of SiO_2 network further facilitate the structural recover from a large compressive strain [39,48]. The PSi-6 aerogel also shows excellent resistance to bending, twisting and cutting (Fig. 2(h)). It is able to be bent into a large deformation and recovered to its original shape as the external loading is removed. In addition, it could be wrapped around a thin stick and tied in a knot without any fracture. Benefiting from the excellent mechanical properties above, the PSi-6 aerogel is machinable and could be cut into any desired shapes by a knife, such as a triangle, hexagon, or shapes of star and flower. Therefore, the synergistic effect between rigid SiO_2 network and flexible PI nanofiber aerogel matrix can significantly improve the mechanical performance of the bulk composites. The PSi aerogel showed enhanced mechanical robustness due to the existence of the stiff silica network and the flexible PI network functioned well in endowing the aerogel with compressive resilience, which is similar to other composite aerogels with “stiff” and “soft” components reported [39,50].

Taking the advantages of the anisotropic structure and integrated double network, the PSi-6 aerogel displayed excellent thermal insulating performance with an ultra-low thermal conductivity of 21.2 mW m^{-1} K^{-1} in the radial direction at 25°C (Fig. 3(a)). As the heat transfer behavior is highly dependent to the pore structure of the materials, thermal conductivity (λ) of PSi aerogels along the radical direction is generally lower than that of the axial direction, which is consistent with other anisotropic thermal insulating materials reported previously [7,51]. According to previous literature, the ratio of axial to radial thermal conductivity is defined as an anisotropic factor, which can be used to quantitatively demonstrate the anisotropic thermal insulation performance of a material [7]. This obvious anisotropy of thermal conductivity is consistent with the anisotropic structure, and the anisotropic factor increases from 1.1 to 6.7 as the value of “x” increased. Moreover, the thermal conductivities of PSi aerogels increase obviously along the axial direction but decreases along the radial direction with the increased silica content. We speculate that the anisotropic multi-scale architecture is responsible for it. Theoretically, the thermal conductivity

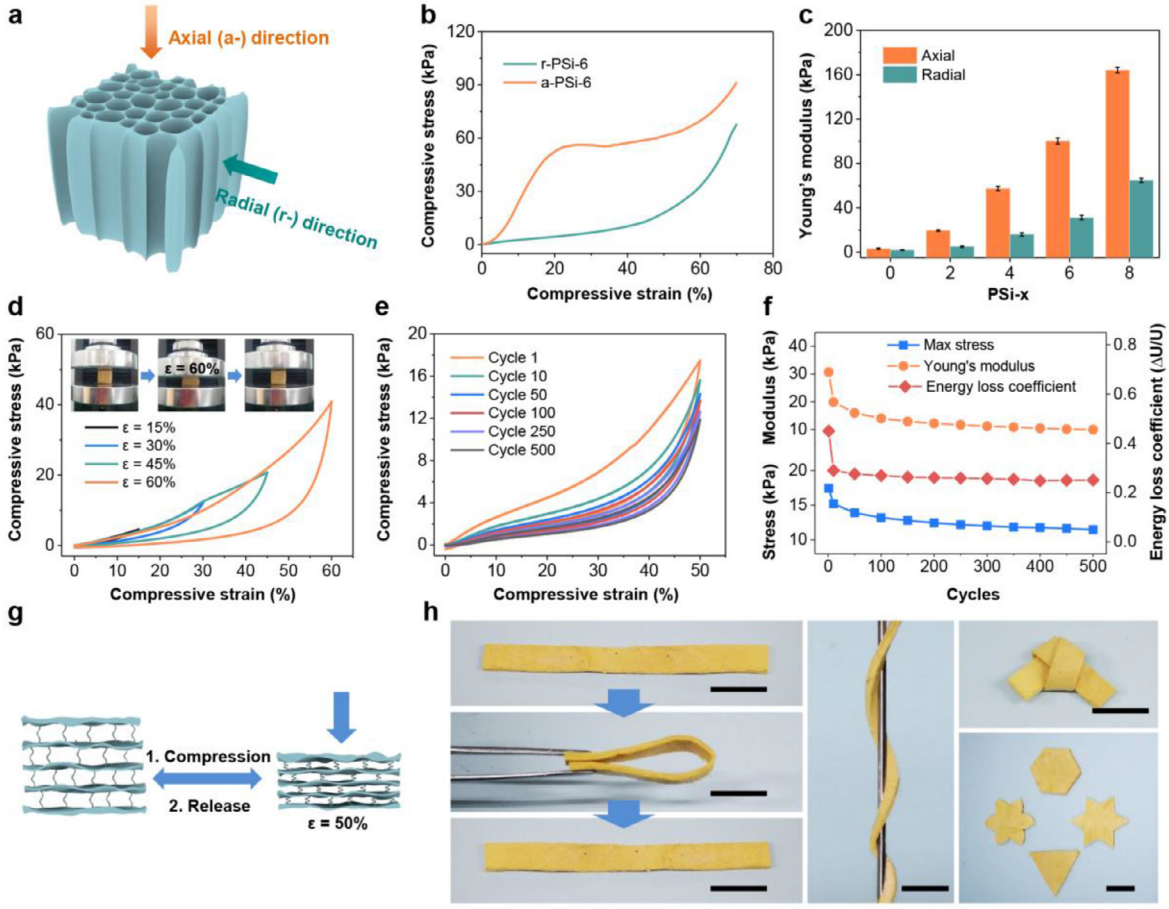

Fig. 2. Mechanical performance of PSi aerogels in the axial and radial directions. (a) Schematic illustration of compression tests performed on the PSi aerogels in the two different directions. (b) Compressive stress-strain curves of the PSi-0 and PSi-6 aerogels in the two directions. (c) Young's modulus of PSi aerogels in the two directions. (d) Compressive stress-strain curves of PSi-6 aerogel during loading-unloading cycles in the radial direction and experimental snapshots of a cycle (inset in d). (e) 500 cyclic compression stress-strain curves of PSi-6 aerogel in the radial direction with a compressive strain of 50%. (f) Variation of Young's modulus, maximum stress and energy loss coefficient versus compressive cycles. (g) Schematic mechanism for the structural robustness and high elasticity of PSi aerogels with cyclic compression in the radial direction. (h) Photographs of PSi-6 aerogel bended and recovered to its original shape, coiled around a plastic rod, knotted and shaped with desired geometry (scale bars are 2 cm).

of porous materials can be recognized as the sum of three contributions related to thermal convection (λ_{conv}), thermal conduction (λ_{cond}) and thermal radiation (λ_{rad}), and thermal conduction consists of solid conduction and gas conduction. Because of the relative low testing temperature and small pore size of PSi aerogels, the radiation and convection contributions are negligible [52]. Thus, solid conduction and gas conduction both contribute to the thermal conductivity in the PSi aerogel. The typical PSi-6 aerogel exhibits a low density of 0.047 g cm^{-3} and an ultra-high porosity of 97.5%, which is beneficial to limit the solid conduction. Three levels of hierarchy at different length scales during the heat conduction process are demonstrated in Fig. 3(b): i) at the macroscale, the anisotropic structure of PSi-6 aerogel facilitated the heat flow along the channel direction, reducing the proportion of the heat flux conducted in the radial direction. ii) At the microscale, the nanofibers between lamellas could form a large number of tortuous heat transmission paths, which were beneficial to decrease the efficiency of heat transfer along the radial direction. iii) At the nanoscale, silica constituents loaded on PINA matrix serve as thermal barriers that provide a significantly increased interfacial thermal resistance, which impede the heat conduction between lamellas and reduce the radial thermal conductivity [53,54]. However, the increased silica content would result in thicker lamellas, which has been proved in Fig. S2a. The thicker lamellas increased solid conduction paths and facilitated the heat transfer along the axial direction, leading to the increase of axial thermal conductivity.

The thermal insulation properties of PSi aerogels were further verified by placing them on the hot stage with different surface temperatures (50, 100, 150, 200°C) and a series of thermographic images were recorded. The two typical images with the stage temperature of 100 and 200°C are shown in Fig. 3(c). The temperature difference (|ΔT|) between the surface of sample and hot stage was measured in Fig. 3(d). The PSi aerogels with increased silica content showed larger |ΔT|, indicating better thermal insulating property and further confirming the conclusions above. Besides, PSi-6 aerogel also exhibited better thermal stability compared with EPS foam when placed on the same hot stage at 200°C. According to the thermographic images taken at different times (Fig. S6(a)), the PSi-6 aerogel exhibited a low average surface temperature of 59.6°C after 30 s owing to its thermal resistance while the EPS foam was already melted, and a larger temperature difference between PSi-6 aerogel and hot stage suggested its better thermal insulation (Fig. S6(b)).

Because of the thermal superinsulation performance of PSi aerogels along the radial direction, we measured the radial thermal conductivities of PSi-6 aerogels under different temperatures (Fig. 3(e)) and relative humidity (Fig. 3(f)). It can be seen from Fig. 3(e) that although the thermal conductivity of PSi-6 aerogel increases with temperature, it still remains quite a low level (below

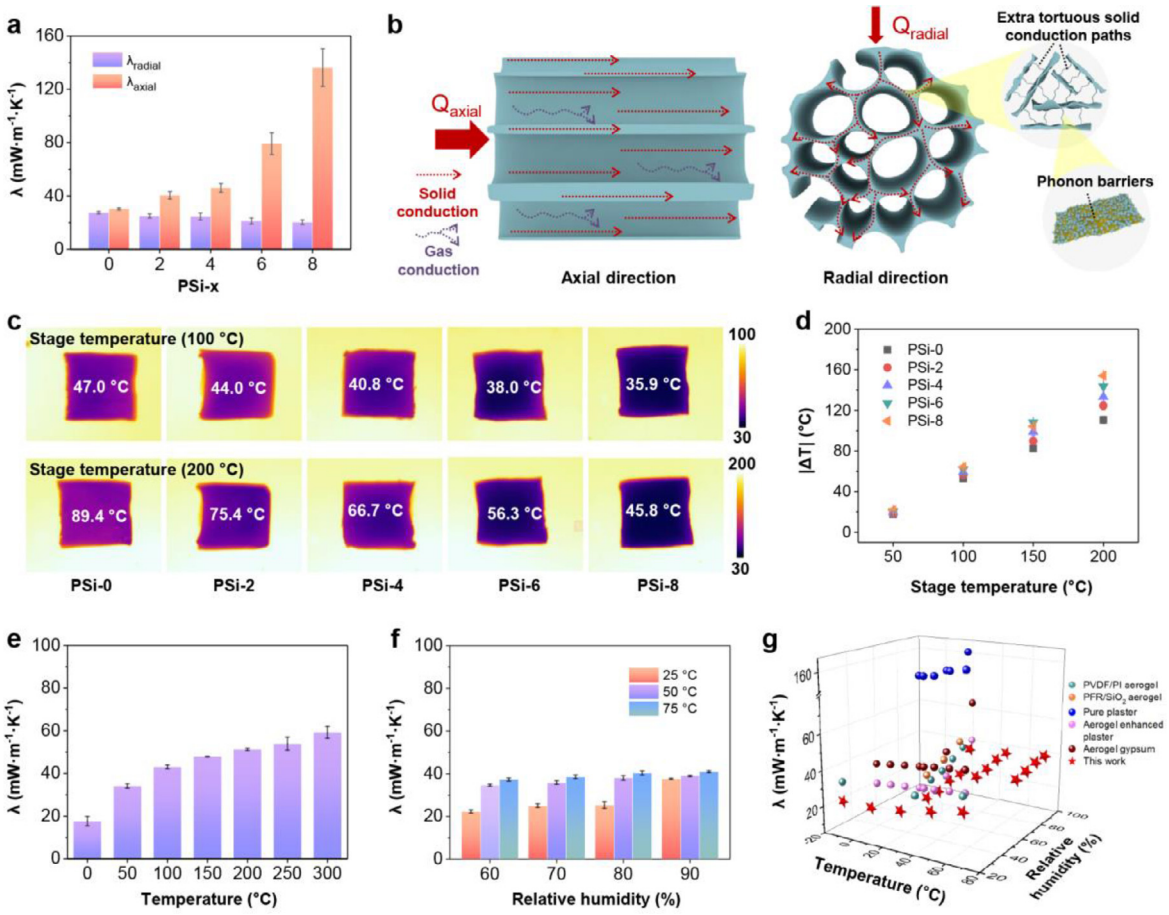

Fig. 3. Thermal insulation properties of PSi aerogels. (a) The thermal conductivities of the PSi aerogels in the axial and radial directions. (b) Schematic illustration indicating the mechanism to achieve excellent thermal insulation. (c) Thermographic images of the PSi aerogels on a hot stage with surface temperatures of 100°C and 200°C. (d) Temperature difference (ΔT) between the PSi aerogels surface and the hot stage with temperatures ranging from 50 to 200°C. (e) The thermal conductivity of the PSi-6 aerogel at different temperatures with constant absolute relative humidity (RH = 34 %). (f) The thermal conductivities of the PSi-6 aerogel at different temperatures and RH. (g) The thermal conductivity of PSi aerogels compared with other insulation materials at different temperatures and relative humidity.

60.0 mW m^{-1} K^{-1}) even at 300°C. Moreover, PSi-6 aerogel displays a high contact angle of 137° (Fig. S7). Due to its hydrophobicity, PSi-6 aerogel exhibits a quite low thermal conductivity of 41.0 mW m^{-1} K^{-1} even at 90 % RH and 75°C, while most commercial insulation materials like EPS or PUR foam tend to exhibit a humidity-dependent thermal conductivity [55]. Moreover, Fig. 3(g) compares the thermal conductivities of PSi aerogels with other thermal insulating materials at different temperatures and relative humidity previously reported, such as PVDF/PI aerogel [38], PFR/SiO_2 aerogel [37], pure plaster, aerogel enhanced plaster and aerogel gypsum [56]. The PSi aerogel exhibits lower thermal conductivities, indicating the great potential for thermal insulating applications in high-temperature and humid environment.

The self-extinguishing property of polyimide and the addition of inorganic constituent allow the composite aerogel to be used as fire-retardant material. As shown in Fig. 4(a)-(c), the EPS foam, PSi-0 and PSi-6 aerogel were burned by an alcohol lamp, respectively. The EPS foam was entirely combusted immediately. The PSi-0 aerogel was ignited by the flame at 20 s and smoldered upon removal of the flame, but occurred a significant volume contraction after a continuous combustion of 60 s. While the PSi-6 aerogel exhibited excellent fire-retardant properties in the flame and no obvious volume change with only charring occurred on the surface of PSi-6 aerogel (Movie S2). The improved flame-retardancy of PSi-6 aerogel is attributed to the integration of silica network and the carbonized PI that can block the external heat entering the interior of aerogel [57]. Fig. S8(a) presented a photograph of the PSi-6 aerogel after combustion, in which the char layer (SiO_2 + carbonized PI) can be clearly observed. During the combustion, the SiO_2 constituents loaded in the PINA matrix served as the first protection layer, which not only limited the transfer of matter such as combustible small molecules and oxygen to the combustion interface, but also delayed the diffusion of heat into the interior [58]. It can be seen from Fig. S8(b) that the char layer exhibited a dense network structure, suggested that this char layer on the surface can act as a thermal barrier during combustion and maintain the integrity of the interior aerogel. The micro-cone calorimetry test was performed on PSi-0, 6 aerogels to study the combustion behavior quantitatively, and the related parameters such as the heat release rate (HRR), peak of heat release rate (PHRR) and total heat release (THR) are summarized. Fig. 4(d) compares the HRR curves of PSi-0 aerogel and PSi-6 aerogel. The HRR curves of PSi-6 aerogel have three heat release peaks. The decomposition of residual methyl groups in silica network led to the first slight HRR peak at ~300 s of PSi-6 aerogel [40]. As the concentration of flammable small molecules and temperature increased, ignition occurred with a rise of HRR to the second peak. A char layer gradually builds up serving as a thermal barrier on the surface of PSi-6 aerogel. Therefore, HRR decreases after the second HRR peak. As the temperature further rose, the char layer starts to crack on the surface, which facilitates the diffusion of small combustible molecules and oxygen into the material. As the cracks grow wider and deeper, HRR

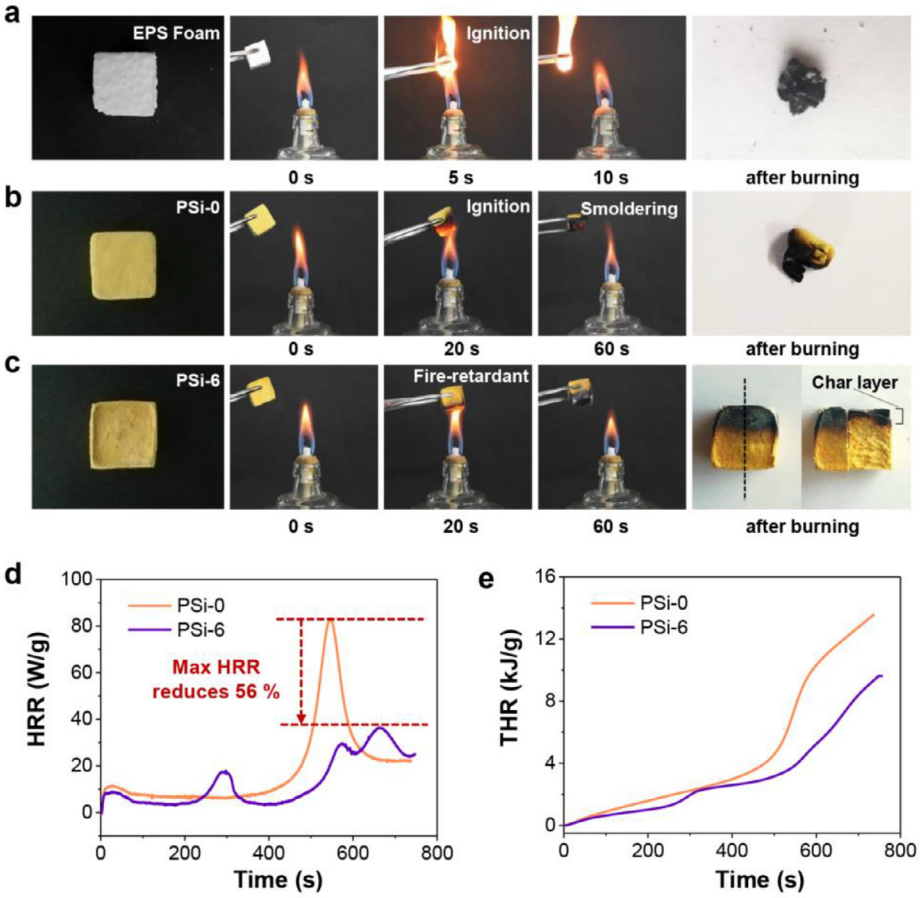

Fig. 4. Flame resistance of PSi aerogels. Photography of (a) EPS foam, (b) PSi-0 and (c) PSi-6 aerogels burning by an alcohol lamp at different times. (d) Heat release rate (HRR) and (e) total heat release (THR) plots of PSi-0 and PSi-6 aerogels during microscale combustion calorimeter testing.

reaches a maximum [59]. The PHRR value of the PSi-6 aerogel (36.1 W g^{-1}) is much lower than that of the PSi-0 aerogel (83.2 W g^{-1}), corresponding to a 56% reduction. Consequently, the total heat release of PSi-6 aerogel (9.6 kJ g^{-1}) is much lower than that of the PSi-0 aerogel (13.6 kJ g^{-1}) (Fig. 4(e)).

To verify the effects of anisotropic structure on flame-resistant performance of the aerogel, the fire resistance tests of PSi-6 aerogels in the axial and radial directions were performed. After combustion test in both directions, the weight loss of the aerogels at different burning times was measured respectively. As shown in Fig. S9, the mass loss rate of the aerogel burned in the radial direction was lower than that in the axial direction. Due to the dense and regularly aligned lamellas could block the ingress of oxygen and the heat transfer, the aerogel was less affected by the flame in the radial direction. To further demonstrate the heat transfer behavior of PSi-6 aerogel in the two directions, the samples are placed on a hot stage with temperature maintaining at 300°C along the axial and radial direction respectively. After 10 min until the sample temperature is stable, the infrared images were taken (Fig. S10). The lower surface temperature of the aerogel placed radially proved that the heat transfer was impeded efficiently along the radial direction.

To further investigate the high-temperature fire-resistance performance of the PSi-6 aerogel, we used a propane/butane blowlamp to simulate the fire with the unrestricted oxygen supply and the thermal images at different times were recorded by an infrared camera (Fig. 5(a)). Since the PSi-6 aerogel exhibits high rigidity only in the axial direction, we performed the combustion test in the axial direction of PSi-6 aerogel to reflect the thermal insulation and flame retardancy of it as an architectural material in fire. Despite the temperature of the front side of the aerogel raised to 1200°C (Fig. 5(b)), the aerogel remained non-combustible and its back side temperature slowly increased to an ultimate temperature of only about 158.3°C after combustion for 30 min (Fig. 5(c)), indicating the superior fire resistance and thermal insulation performance of PSi-6 aerogel. Glass wool, a conventional insulating material, was selected as a comparison sample with the same thickness. Subjecting the glass wool to the propane/butane blowlamp wool resulted in a rapid rise of temperature of 400.8°C after 5 min on the back side and the sample was ultimately burned through by the flame (Fig. 5(d)). The temperature variation curves of these two materials were recorded in Fig. 5(e), which shows the back side temperature of PSi-6 aerogel is always lower than that of glass wool. Furthermore, the PSi-6 aerogel retained its structural integrity even after the continuous combustion. The back side maintained the initial status and the front side was converted into white silica material that was tightly attached to the aerogel (Fig. 5(f)). Remarkably, the silica layer on the front side possesses a continuous network structure as illustrated in Fig. 5(g). This porous structure is responsible for the long-term fire resistant and thermal insulation performance of the aerogel bulk. When the PSi-6 aerogel was subjected to the alcohol lamp flame (~ 550°C), the temperature at the back side was still below 100°C after heating for 5 min and its original structural features maintained(Fig. S11). In addition, PSi-6 aerogel shows exceptional mechanical robustness in the axial direction even after burning with only a slight decrease of Young's modulus (Fig. S12). Owing to the excellent fire resistance, thermal insulation and structural stability in

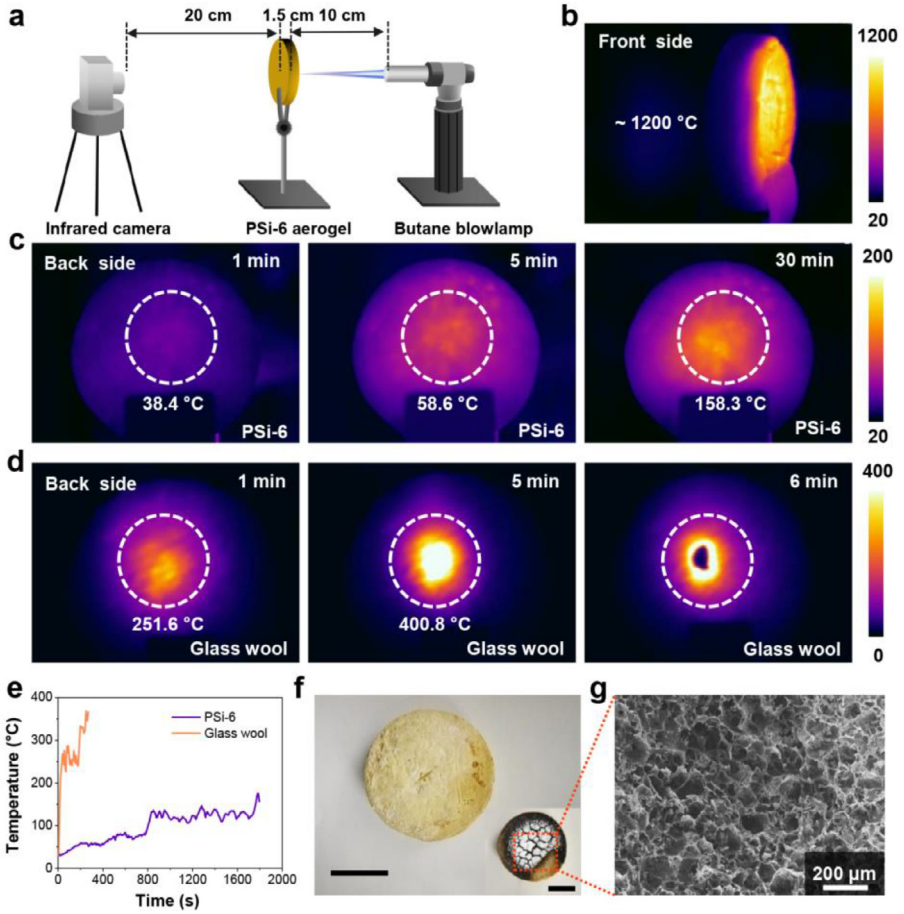

Fig. 5. Fire-retardant and thermal insulation properties of the PSi-6 aerogel in the axial direction under the heating at 1200°C. (a) Schematic of the combustion test performed by butane blowlamp. (b) Thermographic image of the front side exposed to the butane blowlamp flame. (c) Thermographic images of the PSi-6 aerogel back side at different heating times. The average temperature of the circular region is marked. (d) Thermographic images of the back side of the 1.5 cm thick glass wool during heating process. (e) The time-dependent temperature profiles of the back side of the PSi-6 aerogel and glass wool. (f) Photography of the back side of the PSi-6 aerogel after the combustion test. Inset: the front side of the PSi-6 aerogel (scale bars are 5 cm). (g) SEM image of the front side of the PSi-6 aerogel after burning demonstrating the remaining SiO_2 network.

high-temperature flame, PSi composite aerogels are promising candidates as insulation sandwich materials in the exterior walls of architectures.

4. Conclusions

In summary, a novel polyimide-silica (PSi) composite aerogel was fabricated via a straightforward in-situ synthesis strategy that a unidirectional anisotropic PINA was selected as a template for the growth of PMSQ network. The aerogel obtained possesses an anisotropic structure with integrated double network, in which the synergistic effect at different length scales between silica network and PINA matrix endows the PSi aerogels with improved properties, including better thermal stability, higher compressive modulus in the axial direction and excellent compression-recovery property in the radial direction, outstanding thermal insulation property with a low radial thermal conductivity of 21.2 mW m^{-1} K^{-1}. The PSi composite aerogel with 60% silica content exhibits excellent structure stability and integrity when subjected to a flame of ~1200°C, preventing the temperature at non-exposed side from exceeding 200°C. These integrated properties endow the composite aerogel with enormous potential value for architectural, transport and aerospace applications, especially under severe environments where commercial polymeric insulating materials are easily ignited.

Appendix A. Supplementary data

Supplementary material related to this article can be found, in the online version, at doi:

Acknowledgements

This work was supported by the Fundamental Research Funds for the Central Universities (2232019A3-03), the National Natural Science Foundation of China (52073053, 21674019), Shanghai Rising-Star Program (21QA1400300), Shanghai Municipal Education Commission (17CG33), Innovation Program of Shanghai Municipal Education Commission (2021-01-07-00-03-E00108), and Science and Technology Commission of Shanghai Municipality (20520741100).

Supplementary materials

Supplementary material associated with this article can be found, in the online version, at doi:10.1016/j.jmst.2021.07.030.

References

[1] S.B. Sadineni, S. Madala, R.F. Boehm, Renewable Sustainable Energy Rev. 15 (2011) 3617–3631.
[2] D.M.S. Al-Homoud, Build. Environ. 40 (2005) 353–366.
[3] B.P. Jelle, Energy Build. 43 (2011) 2549–2563.

[4] L. Chen, Y.Z. Wang, Polym. Advan. Technol. 21 (2010) 1–26.
[5] R. Baetens, B.P. Jelle, A. Gustavsen, Energy Build. 43 (2011) 761–769.
[6] L. Su, M. Niu, D. Lu, Z.X. Cai, M.Z. Li, H.J. Wang, J. Mater. Sci. Technol. 75 (2021) 1–13.
[7] L. Su, H.J. Wang, M. Niu, S. Dai, Z.X. Cai, B.G. Yang, H.X. Huyan, X.Q. Pan, Sci. Adv. 6 (2020) 6689–6698.
[8] X. Xu, Q.Q. Zhang, M.L. Hao, Y. Hu, Z.Y. Lin, L.L. Peng, T. Wang, X.X. Ren, C. Wang, Z.P. Zhao, C.Z. Wan, H.L. Fei, L. Wang, J. Zhu, H.T. Sun, W.L. Chen, T. Du, B.W. Deng, G.J. Cheng, I. Shakir, C. Dames, T.S. Fisher, X. Zhang, H. Li, Y. Huang, X.F. Duan, Science 363 (2019) 723–727.
[9] B. Chen, Q.F. Zheng, J.L. Zhu, J.H. Li, Z.Y. Cai, L.G. Chen, S.Q. Gong, RSC Adv. 6 (2016) 96518–96526.
[10] H.M. Kim, Y.J. Noh, J. Yu, S.Y. Kim, J.R. Youn, Composites Part A 75 (2015) 39–45.
[11] Q.F. Zheng, A. Javadi, R. Sabo, Z.Y. Cai, S.Q. Gong, RSC Adv. 3 (2013) 20816–20823.
[12] K.P. Ruan, Y.Q. Guo, C.Y. Lu, X.T. Shi, T.B. Ma, Y.L. Zhang, J. Kong, J.W. Gu, Research 2021 (2021) 8438614.
[13] J.W. Gu, Q. Zhang, H. Li, Y. Tang, J. Kong, J. Dang, Polym.-Plast. Technol. Eng. 46 (2007) 1129–1134.
[14] S.H. Ye, B. Wang, Y.T. Shi, B.Z. Wang, Y.R. Zhang, Y.Z. Feng, W.J. Han, C.T. Liu, C.Y. Shen, Compos. Commun. 21 (2020) 100378.
[15] Q.R. Zhang, X.Y. Wang, X.J. Tao, Z.W. Li, X.H. Li, Z. Zhang, Compos. Commun. 15 (2019) 96–102.
[16] B. Wicklein, A. Kocjan, G. Salazar-Alvarez, F. Carosio, G. Camino, M. Antonietti, L. Bergström, Nat. Nanotechnol. 10 (2015) 277–283.
[17] L. Chen, Z.W. Xu, F. Wang, G.G. Duan, W.H. Xu, G.Y. Zhang, H.Q. Yang, J.B. Liu, S.H. Jiang, Compos. Commun. 20 (2020) 100355.
[18] K.P. Ruan, Y. Guo, J.W. Gu, Macromolecules 54 (2021) 4934–4944.
[19] C. Akinyi, J. Longun, S. Chen, J.O. Iroh, Minerals 11 (2021) 168–182.
[20] C. Kizilkaya, Y. Mülazim, M. Vezir Kahraman, N. Kayaman Apohan, A. Güngör, J. Appl. Polym. Sci. 124 (2012) 706–712.
[21] A. Xiang, Y. Li, L. Fu, Y. Chen, H. Tian, A.V. Rajulu, Thermochim. Acta 652 (2017) 160–165.
[22] S.J. Jian, S.S. Liu, L.L. Chen, S.Z. Zhou, P.C. Fan, Y. Zeng, H.Q. Hou, Compos. Commun. 3 (2017) 14–17.
[23] W. Fan, X. Zhang, Y. Zhang, Y.F. Zhang, T.X. Liu, Compos. Sci. Technol. 173 (2019) 47–52.
[24] H. Liu, X.Y. Chen, Y.J. Zheng, D. Zhang, Y. Zhao, C. Wang, C.F. Pan, C.T. Liu, C.Y. Shen, Adv. Funct. Mater. 31 (2021) 2008006.
[25] X.B. Hou, Y.Q. Mao, R.B. Zhang, D.N. Fang, Chem. Eng. J. 417 (2021) 129341.
[26] X.H. Zhang, W. Li, P.Y. Song, B. You, G. Sun, Chem. Eng. J. 381 (2020) 122784.
[27] L.Z. Zuo, W. Fan, Y.F. Zhang, L.S. Zhang, W. Gao, Y.P. Huang, T.X. Liu, Compos. Sci. Technol. 139 (2017) 57–63.
[28] T.T. Xue, W. Fan, X. Zhang, X.Y. Zhao, F. Yang, T.X. Liu, Composites Part B 219 (2021) 108963.
[29] X. Yang, X. Zhong, J. Zhang, J.W. Gu, J. Mater. Sci. Technol. 68 (2021) 209–215.
[30] C. Cao, W. Liu, H. Xu, K. Yu, L. Gong, B. Guo, Y. Li, X. Feng, L. Lv, H. Pan, L. Zhao, J. Li, J. Gao, G. Zhang, L. Tang, J. Mater. Sci. Technol. 85 (2021) 194–204.
[31] B.Q. Wan, H.Y. Li, Y.H. Xiao, Z.B. Pan, Q.W. Zhang, J. Mater. Sci. Technol. 74 (2021) 1–10.
[32] C.B. Liang, Y.X. Liu, Y.F. Ruan, H. Qiu, P. Song, J. Kong, H.B. Zhang, J.W. Gu, Composites Part A 139 (2020) 106143.
[33] S.X. Nie, J.L. Mo, Y.H. Zhang, C.Y. Xiong, S.F. Wang, Carbohyd. Polym. 250 (2020) 116971.
[34] X.H. Zhang, X.X. Ni, C.X. Li, B. You, G. Sun, J. Mater. Chem. A 8 (2020) 9701–9712.
[35] Z. Zhang, X.D. Wang, G.Q. Zu, L. Liu, X.X. Zhang, S. Xi, H.Y. Zhao, J. Shen, J. Supercrit. Fluids. 160 (2020) 104811.
[36] S. Wu, A. Du, Y.L. Xiang, M.F. Liu, T.M. Li, J. Shen, Z.H. Zhang, C.H. Li, B. Zhou, RSC Adv. 6 (2016) 58268–58278.
[37] Z.L. Yu, N. Yang, V. Apostolopoulou-Kalkavoura, B. Qin, Z.Y. Ma, W.Y. Xing, C. Qiao, L. Bergström, M. Antonietti, S.H. Yu, Angew. Chem., Int. Ed. 57 (2018) 4538–4542.
[38] F. Yang, X.Y. Zhao, T.T. Xue, S.J. Yuan, Y.P. Huang, W. Fan, T.X. Liu, Sci. China Mater. 64 (2021) 1267–1277.
[39] J.Y. Zhang, Y.H. Cheng, M. Tebyetekerwa, S. Meng, M.F. Zhu, Y.F. Lu, Adv. Funct. Mater. 29 (2019) 1806407.
[40] X.L. Yuan, L.H. Xu, H. Pan, Y. Shen, L.M. Wang, M.R. Xie, Mater. Res. Express. 8 (2021) 15021–15030.
[41] C. Wang, Z.Z. Pan, W. Lv, B. Liu, J. Wei, X.H. Lv, Y. Luo, H. Nishihara, Q.H. Yang, Small 15 (2019) 1805363.
[42] Z. Yu, T.W. Dai, S.W. Yuan, H.W. Zou, P.B. Liu, ACS Appl. Mater. Interfaces 12 (2020) 30990–31001.
[43] Z.L. Yu, N. Yang, L.C. Zhou, Z.Y. Ma, Y.B. Zhu, Y.Y. Lu, B. Qin, W.Y. Xing, T. Ma, S.C. Li, H.L. Gao, H.A. Wu, S.H. Yu, Sci. Adv. 4 (2018) 7223–7233.
[44] T.P. Peng, J.D. Zhu, T. Huang, C.W. Jiang, F.X. Zhao, S.Z. Ge, L. Xie, J. Appl. Polym. Sci. 138 (2021) 50539–50550.
[45] B. Babiarczuk, D. Lewandowski, A. Szczurek, K. Kierzek, M. Meffert, D. Gerthsen, J. Kaleta, J. Krzak, J. Supercrit. Fluids. 166 (2020) 104997.
[46] Y. Chen, D.B. Fan, S.Y. Lyu, G.Y. Li, F. Jiang, S.Q. Wang, ACS Sustain. Chem. Eng. 7 (2018) 1381–1388.
[47] G.F. Xu, M.J. Li, T.T. Wu, C.Q. Teng, React. Funct. Polym. 154 (2020) 104672.
[48] X.X. Zhang, H.K. Wang, Z.Y. Cai, N. Yan, M.H. Liu, Y. Yu, ACS Sustain. Chem. Eng. 7 (2018) 332–340.
[49] Y. Shen, L.L. Wang, F. Liu, H.Z. Liu, D.W. Li, Q.S. Liu, B.Y. Deng, ACS Appl. Mater. Interfaces 12 (2020) 53104–53114.
[50] Y. Lin, J. Chen, S.A. Dong, G.N. Wu, P.K. Jiang, X.Y. Huang, J. Mater. Sci. Technol. 83 (2021) 219–227.
[51] X. Zhang, X.Y. Zhao, T.T. Xue, F. Yang, W. Fan, T.X. Liu, Chem. Eng. J. 385 (2020) 123963.
[52] F. Hu, S.Y. Wu, Y.G. Sun, Adv. Mater. 31 (2018) 1801001.
[53] M.D. Losego, M.E. Grady, N.R. Sottos, D.G. Cahill, P.V. Braun, Nat. Mater. 11 (2012) 502–506.
[54] K.P. Ruan, X.T. Shi, Y.Q. Guo, J.W. Gu, Compos. Commun. 22 (2020) 100518.
[55] J.B. Alvey, J. Patel, L.D. Stephenson, Energy Build. 144 (2017) 358–371.
[56] R.H. Nosrati, U. Berardi, Energy Build. 158 (2018) 698–711.
[57] F. Laoutid, L. Bonnaud, M. Alexandre, J.M. Lopez-Cuesta, P. Dubois, Mater. Sci. Eng. 63 (2009) 100–125.
[58] J.W. Gu, J. Dang, Y. Wu, C. Xie, Y. Han, Polym-Plast. Technol. Eng. 51 (2012) 1198–1203.
[59] W. Gan, C. Chen, Z. Wang, J. Song, Y. Kuang, S. He, R. Mi, P.B. Sunderland, L. Hu, Adv. Funct. Mater. 29 (2019) 1807444.